Numerical and Experimental Corroboration of an FDTD Thin-Slot Model for Slots Near Corners of Shielding Enclosures

Min Li, Kuang-Ping Ma, David M. Hockanson, *Student Member, IEEE,* James L. Drewniak, *Member, IEEE,* Todd H. Hubing, *Senior Member, IEEE,* and Thomas P. Van Doren, *Senior Member, IEEE*

***Abstract*— Simple design maxims to restrict slot dimensions in enclosure designs below a half-wave length are not always adequate for minimizing electromagnetic interference (EMI). Complex interactions between cavity modes, sources, and slots can result in appreciable radiation through nonresonant length slots. The finite-difference time-domain (FDTD) method can be employed to pursue these issues with adequate modeling of thin slots.**

Subcellular FDTD algorithms for modeling thin slots in conductors have previously been developed. One algorithm based on a quasistatic approximation has been shown to agree well with experimental results for thin slots in planes. This FDTD thin-slot algorithm is compared herein with two-dimensional (2-D) moment method results for thin slots near corners and plane-wave excitation. FDTD simulations are also compared with measurements for slots near an edge of a cavity with an internal source.

***Index Terms*—EMI, FDTD, shielding enclosures, slots.**

I. Introduction

THE integrity of shielding enclosures is compromised by apertures and seams required for heat dissipation, cable penetration, and modular construction, among other possibilities. These perforations allow energy to be radiated to the external environment from interior electronics, or energy coupled from the exterior to interfere with interior circuits. An understanding of energy coupling mechanisms to and from the enclosure is essential to minimize the EMI and susceptibility risk in a new design. Results presented in this paper indicate that simple cavity and antenna theory are inadequate for characterizing power radiated through slots in enclosures. Numerical modeling of enclosure designs can aid in developing enclosure design guidelines. Numerical models have been applied to enclosures for a better understanding of these problems [1], [2]. It is necessary, however, to know the essential features that must be modeled, and to have a proven approach for incorporating the necessary details. The FDTD method has previously been applied for modeling apertures in shielding enclosures as well as attached cables [1]. In these numerical methods, the aperture is typically modeled with widths on the order of the mesh dimension. In order to model a thin slot, or seam, the mesh dimension must be made small in the vicinity of the slot. This can consume significant computational resources. A subcellular capacitive thin slot formalism (C-TSF) for modeling thin slots has previously been introduced by Gilbert and Holland [3]. Previous results for slots in infinite or large planes show this simple and computationally efficient algorithm to agree well with experimental data [4], as well as with a more sophisticated integral-equation based hybrid thin-slot (HTSA) subcellular FDTD algorithm [5], [6]. While C-TSF is formulated and works well for slots in infinite planes, results presented herein show that it is suitable for modeling thin slots near corners of shielding enclosures as well.

The C-TSF, which is based on an equivalent coplanar plate capacitance, was developed to compute the electric field in the slot that is the field averaged over one mesh dimension. As a result, the electric-field component across the slot is significantly underestimated [7]. However, immediately adjacent to the slot, the electric field computed with the C-TSF agrees very well with moment method results, experimental results, and another integral equation based FDTD subcellular method [6], [7]. The C-TSF subcellular method has the advantage of being easily implemented with no additional computational overhead per FDTD time-step. Only the electric and magnetic field components in the slot require modification from the original FDTD time-marching scheme. The resulting algorithm is nearly identical to the usual FDTD equations with the exception that the slot capacitance is incorporated through an effective relative dielectric constant. The slot capacitance for parallel plates is given by an analytical form, and is related to an effective relative dielectric constant.

The C-TSF algorithm is formulated for slots in an infinite plane. However, in many cases, slots are near or on corners. The C-TSF algorithm is employed in this work to model slots $\frac{1}{2}$ FDTD cell off a corner. The present formulation is not suitable for modeling slots exactly on a corner, however, for standard FDTD modeling at $\delta = \frac{\lambda}{20}$, a slot $\frac{\lambda}{40}$ off the corner will behave nearly like that on the corner, since the asymptotic field behavior is dominated by the slot [8]. MOM and experimental results presented herein support this assertion.

The C-TSF FDTD subcellular algorithm is compared with a mixed-potential integral equation formulation in Section II for slots near the corner of a 90° bend in two dimensions

Manuscript received August 19, 1996; revised June 10, 1997.

The authors are with the Department of Electrical Engineering, University of Missouri, Rolla, MO 65409–0710 USA.

Publisher Item Identifier S 0018-9375(97)06434-X.

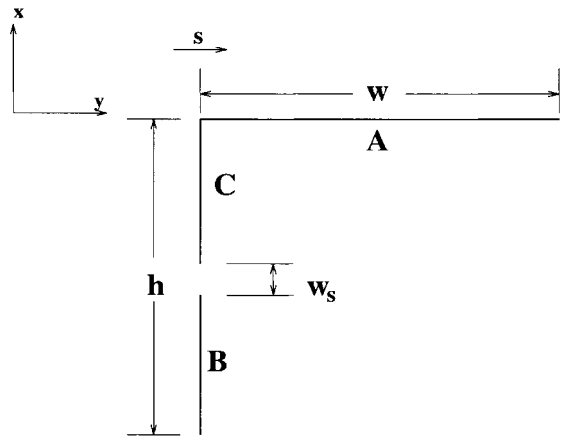

Fig. 1. Geometry for a slot near a corner on a two-dimensional (2-D) finite bent strip.

for a plane wave excitation. In the case of energy coupling through a thin slot with the axis parallel to the z-axis, only the TE_z case is important, since the TM_z case results in orders of magnitude less coupling [9]. A mixed-potential integral equation formulation is employed in order to incorporate the singularity in the charge distribution at the corner for the TE_z case [10]. Several cases of bend geometries are considered, with the slot located near the corner, and in the center of one of the strips. The FDTD results in general agree well with the mixed-potential moment method (MOM) results for the three bend geometries considered when the slot is narrow relative to the FDTD mesh dimension. However, when the slot becomes wide relative to the mesh dimension, the FDTD and MOM results begin to deviate considerably.

FDTD results for thin slots near corners are also compared with measurements in Section III. In this case, EMI modeling of radiation through slots located near corners was of concern. A rectangular conducting enclosure fed with a wire probe was investigated. Necessary modifications to Taflove's thin-wire algorithm for modeling the probe were determined for agreement with the measurements, as well as source and load modeling. Several cases of different slot locations, lengths and widths are presented for a range of weak to strong coupling with the source. In general, the agreement between the measured and experimental results is good.

II. C-TSF and MOM Modeling of Thin Slots Near Corners

The geometry employed for FDTD and MOM comparisons for modeling slots near corners is shown in Fig. 1. The slot was located in two places along one arm of the bent conductor: in the center of one arm; and, one-half cell from the edge. The present formulation of the C-TSF algorithm does not handle slots placed directly on corners, however, for practical purposes, a slot near the corner will result in much the same coupling effects to an enclosure, in particular when modeling at mesh dimensions of $\frac{\lambda}{20}$. Square FDTD cells were employed with $\delta = \delta x = \delta y$. Mesh discretizations of $\delta = \frac{\lambda}{20}$, $\delta = \frac{\lambda}{40}$, and $\delta = \frac{\lambda}{80}$ were used. The bent-strip geometry was illuminated with an x-polarized electric-field incident plane wave with sinusoidal time variation. The FDTD time step was $\delta t = \frac{0.006\,25}{f}$ seconds, where f was the operating frequency. A total-field/scattered-field formulation was used to implement the source [11]. Second-order Mur absorbing boundary conditions were employed for the two-dimensional (2-D) simulations.

The induced surface current density on the conducting strip was calculated from $\overline{\mathbf{J}}_s = \hat{\mathbf{n}} \times \left(\overline{\mathbf{H}}_{lit} - \overline{\mathbf{H}}_{shadow}\right)$, where $\hat{\mathbf{n}}$ is a unit normal vector directed into the lit region, and $\overline{\mathbf{H}}_{lit}$ and $\overline{\mathbf{H}}_{shadow}$ are the magnetic fields in the lit and shadow regions, respectively. For example, the surface current density on Segment B and C is $J_x = H_{zi,jplate} - H_{zi,jplate-1}$. The magnetic-field components $H_{zi,jplate}$ and $H_{zi,jplate-1}$, are the magnetic-field components one half cell away from the strip in the shadow and lit regions, respectively.

A mixed-potential integral equation formulation was also employed for modeling the bent strip for comparison to the FDTD results [10]. In this formulation, a current basis function spans the bend to ensure current continuity, and charge basis functions end at either side of the bend in order to incorporate the singularity in the charge distribution at the corner. A Galerkin's procedure was employed with pulse basis and testing functions. In all cases, 100, 100, and 50 basis functions were used for Segments A, B, and C, respectively, as shown in Fig. 1 [4]. Previous work by Glisson and Wilton has shown that this integral-equation formulation is sufficiently robust to accommodate a large jump in the segment length of the discretization, and no difficulties were encountered in modeling small Segment C pieces with 50 basis functions [10].

FDTD, C-TSF, and MOM results are compared for an $h \times w = 1\ \lambda \times\ 1\ \lambda$ bent strip in Figs. 2 and 3 ($h = B + C + w_s = 1\ \lambda$, and $w = A = 1\ \lambda$). In the figures, the bend is located at $\frac{s}{L} = 0$, and values of $\frac{s}{L} < 0$ denote the strip segment normal to the direction of the incident wave, where s is the length along the strip and L is the wavelength. In both cases, the FDTD mesh dimensions were $\delta = \frac{\lambda}{80}$, and the slot width was $w_s = 0.001\,25\ \lambda = 0.1\ \delta$. The magnitude and phase of the current on the conducting bent strip with the slot in the center of the arm are shown in Fig. 2. In this case, the slot is located where the current maximum would be in the absence of the slot. The FDTD C-TSF subcellular and MOM results in general agree well. The magnitude differs most at the peaks, and there is a discrepancy in the phase around the bend. However, in the region of the slot the agreement is good. The computed current in the FDTD C-TSF case does not go to zero in the slot because this current is computed using values of the magnetic field on both sides of the strip that are displaced one-half cell from the strip. Since the currents on the bent strip agree well, the fields in the vicinity of the slot, as well as away from the strip will agree well also. Results of the current magnitude and phase for a slot located one-half FDTD cell off the corner are shown in Fig. 3. Again the comparison between the FDTD C-TSF subcellular and MOM results is good. In this case the slot is located near a current minima, and has a smaller impact on the current distribution on the bent strip.

Other bent-strip geometries were also considered. In general it is not practical in FDTD modeling to discretize at $\delta = \frac{\lambda}{80}$. This level of detail throughout the computational domain con-

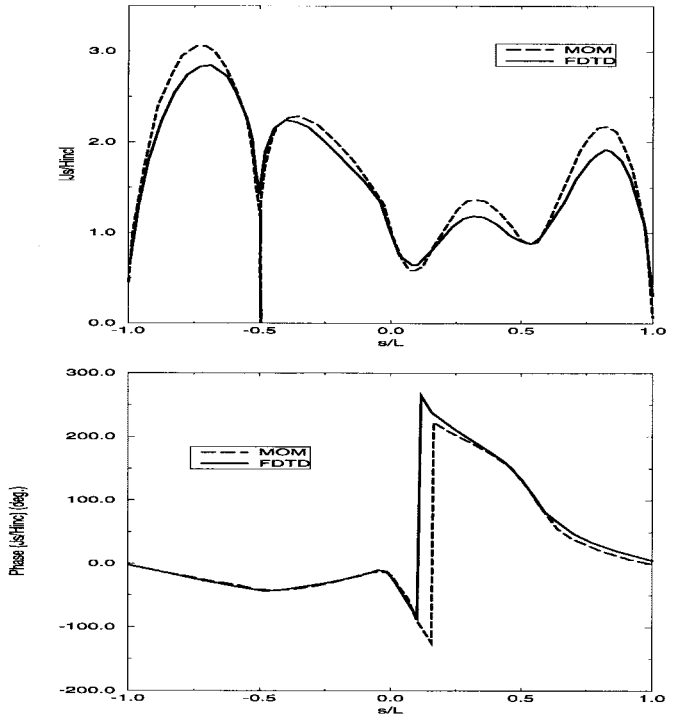

Fig. 2. Comparisons of the magnitude and phase of the induced current on a 2-D bent strip with a thin slot in the center of the $h \times w = 1\ \lambda \times 1\ \lambda$ arm for MOM and FDTD C-TSF.

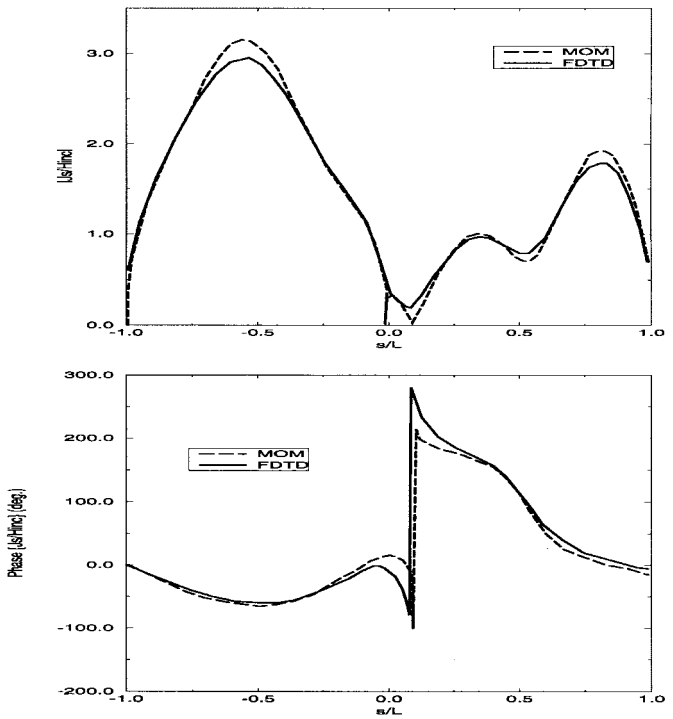

Fig. 3. Comparisons of the magnitude and phase of the induced current on a 2-D bent strip with a thin slot on the corner of the $h \times w = 1\ \lambda \times 1\ \lambda$ arm for MOM and FDTD C-TSF.

sumes excessive memory. In the next case, mesh dimensions of $\delta = \frac{\lambda}{20}$ were employed. In addition, the slot width was changed to $w_s = 0.0002\ \lambda = 0.004\ \delta$. The magnitude of the current on a $h \times w = \frac{\lambda}{2} \times \frac{\lambda}{2}$ bent strip is shown in Fig. 4. Again the results agree well both without and with the thin

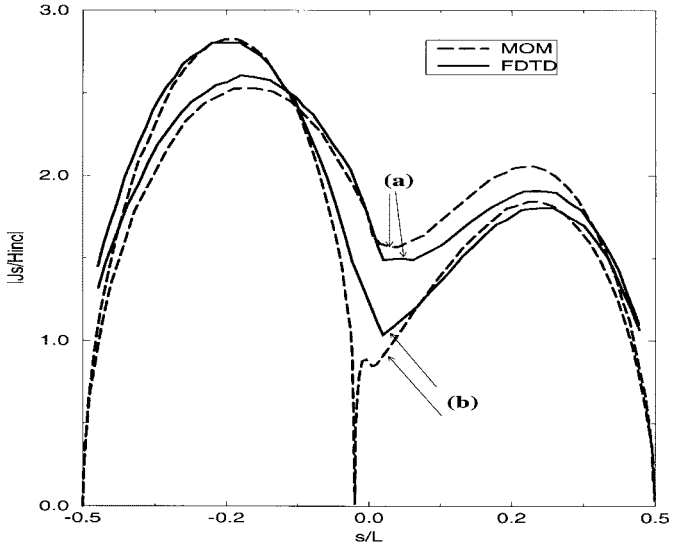

Fig. 4. FDTD C-TSF and MOM comparisons of the magnitude of the induced current on an $h \times w = \frac{\lambda}{2} \times \frac{\lambda}{2}$ 2-D bent strip with (a) no slot and (b) a thin slot on the corner.

slot. Larger slot dimensions for $\delta = \frac{\lambda}{20}$ were also studied with $\frac{w_s}{\delta} = 0.04$ and $\frac{w_s}{\delta} = 0.4$. The MOM and FDTD C-TSF results for $\frac{w_s}{\delta} = 0.04$ agreed well, however, when the slot width was on the order of the mesh dimension for $\frac{w_s}{\delta} = 0.4$, the agreement was poor.

The final case considered was a $h \times w = \frac{\lambda}{4} \times \frac{3\lambda}{4}$ bent strip. In this case the current on the strip without the slot is a maximum near the corner. Introducing the slot and forcing the current to go to zero on the front face of the bent strip significantly alters the current distribution. To allow at least ten FDTD cells to be employed for modeling the $\frac{\lambda}{4}$ bent strip, a mesh dimension of $\delta = \frac{\lambda}{40}$ was used. The slot width was changed as well so that $\frac{w_s}{\delta} = 0.004$, as in the previous case. The FDTD C-TSF and MOM results without and with a slot are shown in Fig. 5. The results still agree well even when the thin slot is introduced near a current maximum on the strip. As in previous cases, when the slot width is on the order of the mesh dimensions $\frac{w_s}{\delta} = 0.4$, the agreement is poor.

III. FDTD and Experimental Results

Measurements were pursued in order to assess the accuracy of modeling thin slots near corners with C-TSF in 3-D. The geometry of the experimental conducting enclosure is shown in Fig. 6. The cavity was fed with a 50 Ω coaxial cable probe through a type-N bulkhead connector, which was peripherally bonded to the cavity. The center conductor of the probe was extended to span the width of the cavity with a 0.16 cm diameter wire, and terminated on the opposite cavity wall with a 1206 package size surface-mount (SMT) 47 Ω resistor soldered to a 1.5×1.5 in square of conductive adhesive copper tape. The feed probe was located at $x = 17$ cm, $y = 14$ cm, $z = 15$ cm. The SMT resistor was characterized with an HP4291A impedance analyzer and HP16192A SMT test fixture over the frequency range of the measurements. The magnitude of the impedance was a constant 47 Ω with $|X| < 3\ \Omega$ of reactance.

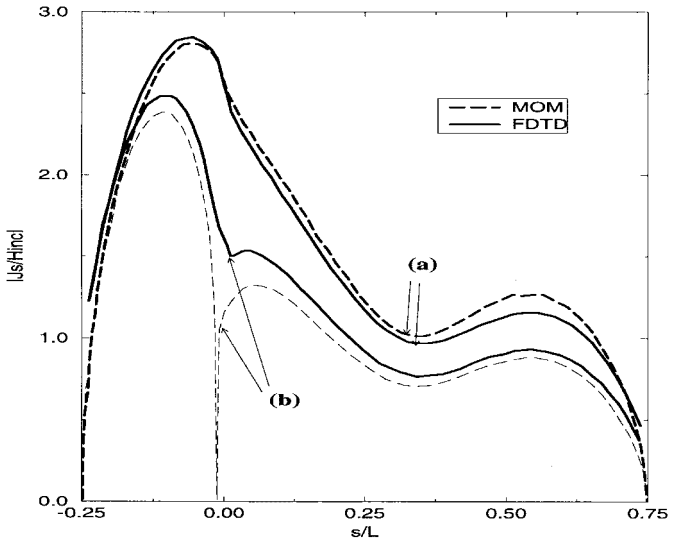

Fig. 5. FDTD C-TSF and MOM comparisons of the magnitude of the induced current on an $h \times w = \frac{\lambda}{4} \times \frac{3\lambda}{4}$ 2-D bent strip with (a) no slot and (b) a thin slot on the corner.

The cavity was constructed of five pieces of 0.635 cm thick aluminum, and one plate of 0.05 cm thick aluminum for the face containing the slot. The cavity was constructed so that it could easily be disassembled and reassembled for repeatable measurements. The inside dimensions of the enclosure were 22 × 14 × 30 cm. One-inch copper tape with conductive adhesive was used to electromagnetically seal the seams. Several experiments were conducted with different positions of the slot as well as varying the slot length and width. The frequency range of the measurements was 700 MHz to 1.6 GHz in order to excite several cavity modes, slot modes, and the feed-probe TEM mode.

A Wiltron 37247A network analyzer was employed to measure the reflection coefficient S_{11}, and the real power delivered by the source was calculated from the one-port measurements. From simple transmission-line theory, the real power delivered to the test port of the enclosure is

$$P = \frac{1}{2} Re\{\hat{V}(\ell)\hat{I}^*(\ell)\} = \frac{|\hat{V}_s|^2}{8Z_0}(1 - |\hat{\Gamma}_L|^2) \quad (1)$$

where Z_0 is the characteristic impedance of the test port, and $\hat{V}_s$ is the source voltage. The source voltage is normalized to $1\,V$ for comparison with the FDTD results (that employ a $1\,V$ source). For one-port measurements, the reflection coefficient $\hat{\Gamma}_L = \hat{S}_{11}$, and

$$P = \frac{1}{8Z_0}(1 - \hat{S}_{11}^2). \quad (2)$$

A cell size of 1.0 × 0.5 × 1.0 cm was employed in the FDTD simulations, where finer discretization along the y direction was used in order to better model the spatial extent of the SMT load resistor. Aluminum plates were modeled with PEC surfaces by setting the tangential electric field to zero on the cavity walls. The feed probe was modeled by a simple voltage source V_s with 50 Ω resistance incorporated into a single cell at the feed point. The magnetic fields circling the source were modeled in the same fashion as a thin wire to give the cross-section of the source specified physical dimensions [12]. The resistor was modeled as a lumped element using a subcellular algorithm [13]. The width of the SMT is approximately that of the feed wire diameter, and the physical cross-section dimensions were modeled with the same diameter as that of the feed wire by modifying the magnetic field components circling the SMT in the same fashion as for the source. The slot was modeled with the C-TSF, and Perfectly-Matched-Layer (PML) absorbing boundary conditions were employed for the 3-D simulations [14]. The PML absorbing layers were four cells away from the PEC planes without the slot, and eight cells away from the PEC planes containing or near the slot.

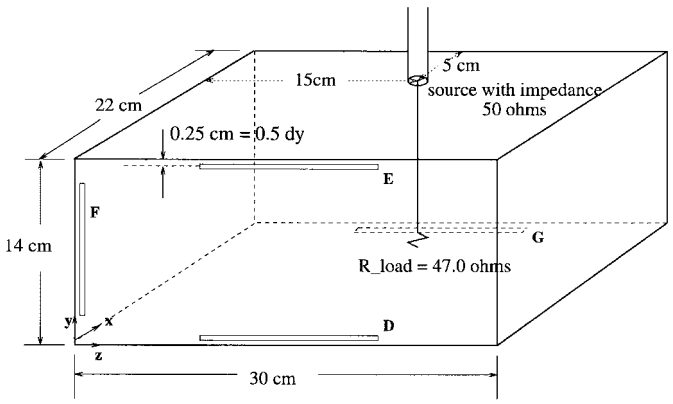

Fig. 6. Shielding enclosure geometry for comparison of FDTD and measured results.

A sinusoidally modulated pseudo-Gaussian pulse was employed as the excitation. The source voltage as a function of time t was

$$V_s(t) = e^{-\alpha_1^2(f_2-f_1)^2(t-\frac{\alpha_2}{f_2-f_1})^2} cos[2\pi \frac{f_1+f_2}{2}(t - \frac{\alpha_2}{f_2-f_1})] \quad (3)$$

where f_1 and f_2 are the starting and stopping frequencies of the simulation, respectively, and α_1 and α_2 are constants ($\alpha_1 = 1.035$ and $\alpha_2 = 2.539$). This time-variation and constants were chosen so that the temporal pulse was greater than two orders of magnitude below maximum at the beginning and end of the pulse. Also the DC component of the transformed signal was several orders of magnitude less than the signal level at the bandwidth boundaries f_1 and f_2. The argument in the modulating cosine was chosen to shift the pulse in frequency to the center of the desired bandwidth $\frac{f_1+f_2}{2}$. A time step of $8.3333\,ps$ was employed. The time-history of the voltage V_0 across the source and source impedance, and the current I_0 through the source were stored, and a Fast Fourier Transformation (FFT) was employed to obtain frequency-domain quantities. A total of 20 000 time steps was required for a good resolution in the frequency domain. In simulations with frequency bands containing very high Q resonances, e.g., 1.36 GHz in Fig. 8(a), an additional 20 000 time steps, or 40 000 total were required in order for the stored energy to decay and minimize ringing. The computed real power delivered by the

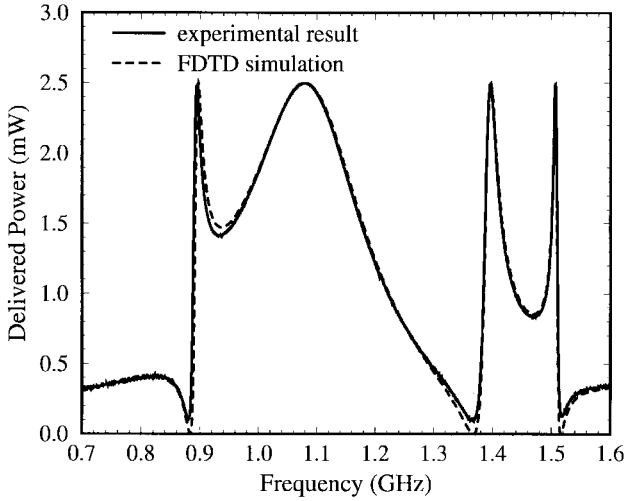

Fig. 7. Comparison of experimental and FDTD results for the continuous cavity (no slot).

source was calculated as

$$P_{FDTD} = \frac{1}{2} Re(\hat{V}_0 \times \hat{I}_0^*). \tag{4}$$

The configuration without the slot was studied first to determine the cavity resonances, and to develop accurate models of the source, feed probe and termination. The experimental and FDTD results are shown in Fig. 7. Since a 1 V, 50 Ω source was employed, the maximum power available at the source terminals was 2.5 mW. The physical radius of the feed-probe wire was 0.08 cm, and Taflove's thin-wire subcellular algorithm was employed for modeling the wire radius. However, employing the physical radius of the wire resulted in a frequency shift of the FDTD results of 0.5-1.5% for all resonances, including the broad feed-probe (TEM) resonance at 1.08 GHz. The FDTD computed cavity and feed-probe resonances were compared to the experimental data for varying effective wire radius. An effective radius of 70% of the physical radius yielded almost identical results between the experiments and FDTD for the closed cavity. Previous FDTD modeling showed a similar frequency shift when employing this thin-wire algorithm for modeling open radiating structures [12].

Since the feed-probe wire was along the y direction, the y-component of the electric field was excited, while the y-component of the magnetic field was suppressed, i.e., only TM_y cavity modes were excited by the feed probe. The time histories of the fields at six random points inside the cavity were recorded in one set of FDTD simulations. The results of H_y in the time domain were only computational round-off error, which was four orders of magnitude below the peak value of H_x and H_z. Resonances at 0.89 GHz, 1.40 GHz, and 1.51 GHz correspond to the TM_y101, TM_y111 and TM_y201 modes, respectively. They are 5%, 3%, and 4%, respectively, higher than the frequencies of ideal cavity resonances. The resonance at 1.08 GHz is a result of the terminated feed probe, and corresponds to a TEM mode. The current distribution on the feed wire at 1.08 GHz was a $\frac{\lambda}{2}$ standing wave. Since the "transmission line" is $\frac{\lambda}{2}$ (half-wavelength window), and the load is near matched to the 50 Ω source, the power delivered to the load is approximately the available power. The good agreement between experimental and simulated results show that the wall loss is negligible since surface impedance was not incorporated in the FDTD simulation. Further, the wall loss for the TM_y101 mode (which is identical to the TE_z101 mode) can be calculated from the aluminum conductivity and the electric field in the center of the cavity [15], and the latter can be obtained from FDTD simulations. The calculated wall loss is less than 0.5% of the total power loss. The terminating resistor is a much more significant loss mechanism than the wall loss for the configuration investigated.

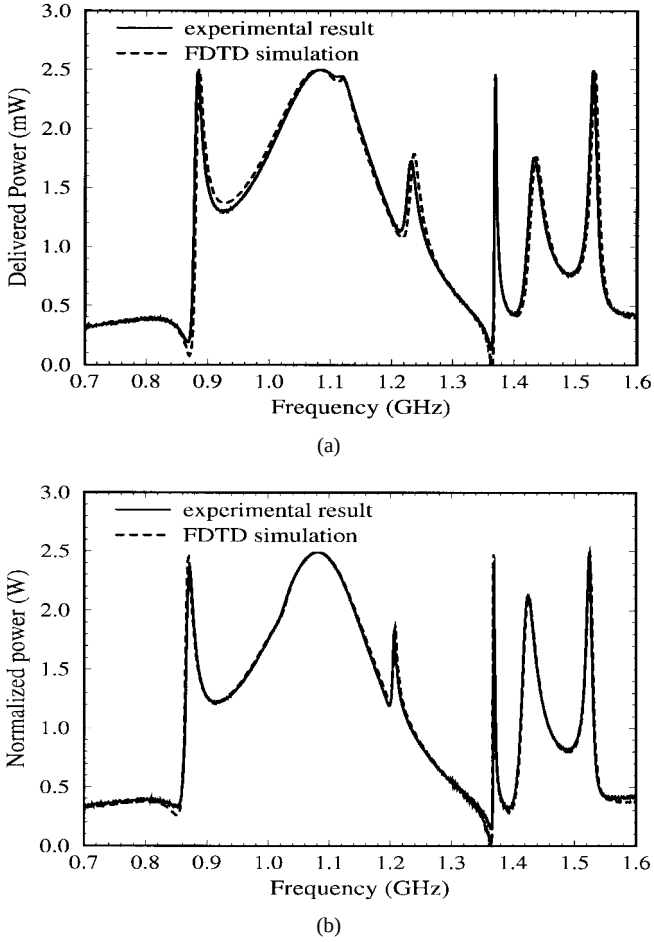

Fig. 8. Comparison of experimental and FDTD results for a slot at Position D, (a) with a slot length of 12 cm and width of 0.1 cm, and (b) with a slot length of 14 cm and width of 0.1 cm.

Several configurations of slots near corners were simulated and measured. The specific slot locations were chosen to demonstrate the adequacy of the C-TSF for a range of excitation of the slot, from weak to strong, as well as proximity to the source. FDTD and experimental results are compared in Fig. 8(a) for a slot of width 0.1 cm ($\frac{w_s}{\delta y} = 0.2$) and length of 12 cm. The center of the slot was 0.25 cm $= \frac{1}{2}\delta y$ from the bottom edge at Position D. Overall, the simulated and experimental results in Fig. 8(a) agree well. The TM_y101 cavity mode is at 0.89 GHz. Resonances at 1.36 GHz and 1.44 GHz correspond to the TM_y111 and TM_y201 modes, respectively. The resonances at 1.12 GHz and 1.24 GHz are

due to the slot because they disappear in both the experiments and simulations when the slot is eliminated. The resonance at 1.54 GHz is believed to be due to the slot. Calculations from the FDTD simulations of the power dissipated in the load resistor show that most of the power delivered by the source is radiated through slot at this resonance. The resonance at 1.24 GHz is the half-wavelength frequency (slightly lower for a finite width slot). The resonances at 1.12 GHz and 1.54 GHz result from interaction of the slot with the feed probe or cavity, and tuning of the reactance [16]. These resonances can not be explained by simple half-wavelength antenna theory, and are presently not well understood. The peak in the power delivered by the source at 1.12 GHz, 1.24 GHz, and 1.54 GHz results in significant radiation from the slot. Calculations from FDTD simulations of the power dissipated in the load resistor and total power show that 28%, 60%, and 89% of the delivered power was radiated through the slot at 1.12 GHz, 1.24 GHz, and 1.54 GHz, respectively.

The FDTD simulated cavity mode resonances were slightly shifted to higher frequencies as compared to the measurements with a shift less than 0.3%, which was within the experimental error. The 0.6% shift of the half-wave slot resonance at 1.24 GHz, however, could not be explained by experimental error. It may be due to the inherent 2-D nature of the C-TSF thin-slot algorithm. The HTSA subcellular algorithm for modeling the slot was also employed [5], [6], in order to investigate the shift in the slot resonance at 1.24 GHz. HTSA, while more complicated to implement than C-TSF, has the advantage that it is inherently three dimensional, and the slot depth is modeled. The resulting data for the frequency band around the slot resonance at 1.24 GHz (as well as over the rest of the frequency range) computed with HTSA agreed well with the measurements. Instability occurred in simulations employing HTSA after 4000 time steps because the width of the slot herein is on the order of the spatial step used in the transient integral equation solution in HTSA. So HTSA was employed only to study the effects of the 2-D nature of the C-TSF FDTD algorithm near the slot half-wavelength resonance. In the initial comparisons employing HTSA, an equivalent radius for zero slot depth was employed. These results agreed almost exactly with the measurements around the slot half-wave resonance. Including the slot depth of 0.05 cm in HTSA showed little discernible difference as compared to a zero slot depth [17]. Therefore the difference between the HTSA and C-TSF implementation of the slot was attributed to the former being a 3-D, and the latter a 2-D formulation. In the C-TSF algorithm, the thin slot is viewed as a 2-D coplanar, parallel strip capacitor in the plane perpendicular to the slot, and slowly varying field quantities across the slot direction are assumed. The slot can then be modeled by modifying the relative permittivity and relative permeability in the FDTD algorithm. In the HTSA algorithm, a slot in a PEC screen is modeled by an equivalent magnetic current source, and replacing the perforated screen with a solid screen, using equivalence and image principles. The formulation is inherently 3-D and can incorporate the slot thickness.

The previous configuration with a 14 cm slot length at Position D was also investigated. In this case, the thickness of the thin aluminum plate with the slot was 0.07 cm. From HTSA simulated results, the effect of the 0.07 cm slot depth as compared to a 0.05 cm slot depth for the half-wave slot resonance was shifted to higher frequency by less than 0.1%, and the 0.07 cm slot depth had little effect. The experimental and FDTD results for the 14 cm slot at Position D are shown in Fig. 8(b). The longer slot length shifted the previous slot resonances at 1.12 GHz, 1.24 GHz, and 1.54 GHz to lower frequencies at 1.02 GHz, 1.21 GHz, and 1.52 GHz, respectively, as expected. The slot resonance at 1.02 GHz was only a small effect in both the measurements and simulation, and dominated by the TEM mode resonance. However, the power radiated through the slot calculated from the simulated results at this resonance was still significant. The power radiated through the slot was 20%, 53%, and 79% of the delivered power at 1.02 GHz, 1.21 GHz, and 1.52 GHz, respectively. The feed-probe resonance at 1.08 GHz was unaffected by the increased slot length. The FDTD simulation showed that the power radiated through the slot at the TM_y101 cavity resonance increased from 12% to 33% of the power delivered by the source, even though the slot was only 0.35 λ at the TM_y101 frequency.

A 12 cm length slot with a width of 0.1 cm ($\frac{w_s}{\delta y} = 0.1$), and located 0.25 cm $= \frac{1}{2}\delta y$ from the center of the slot to the edge near the enclosure top at Position E was also studied. The measured and simulated results are shown in Fig. 9(a). The power delivered to the enclosure at the feed-probe resonance remained the same, while the levels at 1.12 GHz, 1.24 GHz, and 1.53 GHz, at which significant energy was radiated through the slot for Position D, were reduced. The power radiated through the slot was reduced to 18%, 32%, and 36% of the power delivered by the source, at 1.12 GHz, 1.24 GHz, and 1.53 GHz, respectively.

A 12 cm long slot with a width of 0.158 cm ($\frac{w_s}{\delta z} = 0.158$) and 0.5 cm$= \frac{1}{2}\delta z$ from the center of the slot to the edge at Position F was also investigated. In this case, the slot axis is parallel to the feed-probe. The measured and simulated results are the same as the results for the configuration when the slot was eliminated, shown in Fig. 7. The cavity modes TM_y101, TM_y111, TM_y201 and feed-probe mode were excited at the same frequencies as when the enclosure had no slot. For the slot at Position F, there is no magnetic field component along the slot direction inside the cavity, which means that there is no current perpendicular to the slot on the cavity face containing the slot. So the current distribution in the cavity is virtually undisturbed by introducing the slot, and the slot resonance is not excited, nor does the slot interact with the cavity or feed probe in this frequency range.

A 12 cm length slot with a width of 0.158 cm ($\frac{w_s}{\delta x} = 0.158$), and located 0.5 cm $= \frac{1}{2}\delta x$ from the center of the slot to the edge was placed on the bottom face at Position G. It was expected that the coupling between the slot and source probe wire would be stronger in this situation, since the feed-probe and slot were in close proximity. The experimental and simulated results shown in Fig. 9(b) indicate significant coupling between the feed probe and slot. The feed-probe resonance occurs at a lower frequency of 1.03 GHz. The previous slot resonances at 1.12 GHz and 1.24 GHz shifted to

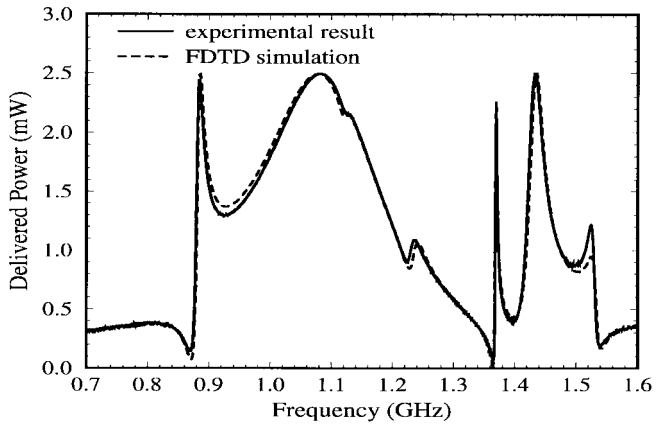

(a)

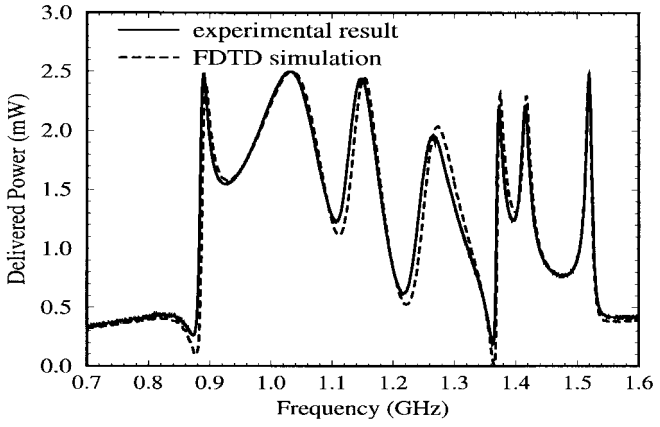

(b)

Fig. 9. Comparison of experimental and FDTD results for a slot length of 12 cm and width of 0.158 cm: (a) at Position E and (b) at Position G.

higher frequencies at 1.15 GHz and 1.27 GHz, respectively. The power radiated through the slot also increased to 40% and 52% of the power delivered by source, at 1.15 GHz and 1.27 GHz, respectively. The slot half-wave resonance was also broadened in frequency, with a half-power bandwidth more than twice that of the previous cases.

IV. Conclusion

A capacitive thin-slot formalism proposed by Gilbert and Holland for subcellular FDTD modeling has been implemented and compared with a mixed-potential integral equation formulation and measurements for modeling thin slots near corners. The case of a 2-D bent strip was considered for several strip configurations. In general, the agreement was good for slot widths small relative to the mesh dimensions $\frac{w_s}{\delta} \leq 0.2$. So for the C-TSF algorithm formulated for thin slots in infinite planes, the effect of the corner for a thin slot near a corner is negligible. For slot widths $\frac{w_s}{\delta} > 0.2$, the agreement deteriorates. In these cases, there is little advantage to a subcellular algorithm. Further, modeling a slot with a single FDTD cell may not adequately represent the field behavior around the slot. In the case when a slot is on the order of a mesh dimension, a multi-grid or other suitable approach is necessary to adequately model the field behavior in the region of the slot.

FDTD modeling of thin slots near corners with C-TSF was also compared with experimental results for a three-dimensional enclosure. The agreement was good for the range of weak to strong interaction of the slot and feed probe. The coupling was strong when the slot was near the load resistor and in the face of the termination, while no coupling resulted for the case that the slot was parallel with the feed-probe wire. The half-wave resonance of the slot modeled with C-TSF was in general shifted up in frequency as compared to the measurements by approximately 0.5% for lower Q resonances. For a high-Q resonance as at 1.24 GHz in Fig. 8(b), the agreement is good. In general, from an EMI perspective this slight shift for low-Q resonances is not a significant disadvantage. The shift is not so great that a clock harmonic might occur at a resonant frequency indicated by simulations and not the experimental situation, i.e., predicting a problem where one does not exist. Conversely, the shift is not so great that a problem might occur and not be predicted.

Accurate modeling of the source, feed-wire, and termination resistor were also pursued. Previously reported subcellular algorithms were employed for modeling each. However, comparison with the measured results demonstrated that the magnetic fields circling the conduction current path must be modified for the source, feed-wire, and SMT resistor employing an effective radius for the conduction current path. The effective radius was 70% of that of the physical radius of the feed-probe wire.

The results from this study show that significant power can be radiated for slots less than a half-wavelength. In one case nearly a third of the power available at the source terminals was radiated through a 0.35 λ length slot at an enclosure resonance. In design, attempts are made at breaking up large enclosures that might support many modes at the highest frequency of concern by introducing conducting subcompartments within the larger enclosure. The idea is to increase the frequency of the fundamental cavity mode. Simple antenna and cavity mode theory, however, are inadequate for anticipating coupling between the source and slot, and reactive tuning between a slot and cavity, or slot and source. These mechanisms can lead to EMI problems not predicted by simple theories. Though these mechanisms are currently not well understood, FDTD simulations that adequately model the necessary features of the enclosure, source, and slot can predict more complicated interactions, and lead to a better understanding of coupling between cavity modes, sources and slots.

References

[1] D. Hockanson, J. L. Drewniak, T. H. Hubing, and T. P. VanDoren, "Application of the finite-difference time-domain method to radiation from shielded enclosures," in *Proc. IEEE Electromag. Compat. Symp.*, Chicago, IL, 1994, pp. 83–88.

[2] M. S. Tharf and G. I. Costache, "A hybrid finite element—analytical solutions for inhomogeneously filled shielding enclosures," *IEEE Trans. Electromag. Compat.*, vol. 36, pp. 380–384, Nov. 1994.

[3] J. Gilbert and R. Holland, "Implementation of the thin-slot formalism in the finite-difference EMP code THREDII," *IEEE Trans. Nucl. Sci.*, vol. NS-28, pp. 4269–4274, Dec. 1981.

[4] K.-P. Ma, "Numerical Simulations for Thin Slot Penetration," M.S. thesis, Univ. Missouri-Rolla, 1995.
[5] D. J. Riley and C. D. Turner, "Hybrid thin-slot algorithm for the analysis of narrow apertures in finite-difference time-domain calculations," *IEEE Trans. Antennas Propagat.*, vol. 38, pp. 1943–1950, Dec. 1990.
[6] K.-P. Ma, M. Li, J. L. Drewniak, T. H. Hubing, and T. P. Van Doren, "A comparison of FDTD algorithms for subcellular modeling of slots in shielding enclosures," *IEEE Trans. Electromag. Compat.*, vol. 39, pp. 147–155, May 1997.
[7] C. D. Turner and L. D. Bacon, "Evaluation of a thin-slot formalism for finite-difference time-domain electromagnetic codes," *IEEE Trans. Electromag. Compat.*, vol. 30, pp. 523–528, Nov. 1988.
[8] R. Mitta and S. W. Lee, *Analytical Techniques in the Theory of Guided Waves*. New York: Macmillan, 1971.
[9] C. M. Butler, "A formulation of the finite-length narrow slot or strip equation," *IEEE Trans. Antennas Propagat.*, vol. AP-30, pp. 1254–1257, Nov. 1982.
[10] A. W. Glisson and D. R. Wilton, "Simple and efficient numerical methods for problems of electromagnetic radiation and scattering from surfaces," *IEEE Trans. Antennas Propagat.*, vol. AP-28, pp. 593–603, Sept. 1980.
[11] A. Taflove, *Computational Electrodynamics*. Boston, MA: Artech House, 1995.
[12] D. M. Hockanson, J. L. Drewniak, T. H. Hubing, and T. P. Van Doren, "FDTD modeling of common-mode radiation from cables," *IEEE Trans. Electromag. Compat.*, vol. 38, pp. 376–387, Aug. 1996.
[13] Y.-S. Tsuei, A. C. Cangellaris, and J. L. Prince, "Rigorous electromagnetic modeling of chip-to-package (first-level) interconnections," *IEEE Trans. Comp., Hybrids, Manufact. Technol.* vol. 16, pp. 876–882, Dec. 1993.
[14] J. P. Berenger, "Perfectly matched layer for the absorption of electromagnetic waves," *J. Comput. Phys.*, vol. 114, pp. 185–200, Oct. 1994.
[15] C. A. Balanis, *Advanced Engineering Electromagnetics*. New York: Wiley, 1989.
[16] C.-H. Liang and D. K. Cheng, "Electromagnetic fields coupled into a cavity with a slot-aperture under resonant conditions," *IEEE Trans. Antennas Propagat.*, vol. AP-30, pp. 664–672, July 1982.
[17] R. P. Jedlicka, S. P. Castillo, and L. K. Warne, "Experimental study of narrow slot, cavity-backed apertures with finite wall conductivity," in *Proc. Antennas Propagat. Soc. Symp.*, 1991, vol. 2, pp. 889–892.

Min Li, for a photograph and biography, see p. 155 of the May 1997 issue of this TRANSACTIONS.

Kuang-Ping Ma, for a photograph and biography, see p. 155 of the May 1997 issue of this TRANSACTIONS.

David M. Hockanson (S'90) received the B.S. and M.S. degrees in electrical engineering from the University of Missouri, Rolla, in 1992 and 1994, respectively.

His research interests include the numerical and experimental analysis of electromagnetic compatibility problems. Previous work has involved digital power bus design and shielding enclosure design. Presently he is working on experimental investigations and equivalent circuit development of noise sources and radiation mechanisms on printed circuit board geometries. His research and education endeavors have been supported by scholarships, fellowships, and assistantships, the most recent being a National Science Foundation Graduate Fellowship.

James L. Drewniak (S'85–M'90), for a photograph and biography, see p. 155 of the May 1997 issue of this TRANSACTIONS.

Todd H. Hubing (S'82–M'82–SM'93), for a photograph and biography, see p. 155 of the May 1997 issue of this TRANSACTIONS.

Thomas P. Van Doren (S'60–M'69–SM'97), for a photograph and biography, see p. 155 of the May 1997 issue of this TRANSACTIONS.